Simulated Clear-Sky Water Vapor and Temperature Retrievals from PREFIRE Measurements

NATHANIEL B. MILLER,[a,b] ARONNE MERRELLI,[c] TRISTAN S. L'ECUYER,[b,d] AND BRIAN J. DROUIN[e]

[a] *Space Science and Engineering Center, Madison, Wisconsin*
[b] *Cooperative Institute for Meteorological Satellite Studies, Madison, Wisconsin*
[c] *Department of Climate and Space Sciences and Engineering, University of Michigan, Ann Arbor, Michigan*
[d] *University of Wisconsin–Madison, Madison, Wisconsin*
[e] *Jet Propulsion Laboratory, California Institute of Technology, Pasadena, California*

(Manuscript received 25 October 2022, in final form 21 February 2023, accepted 9 March 2023)

ABSTRACT: The Polar Radiant Energy in the Far Infrared Experiment (PREFIRE) mission will measure Earth's emission at wavelengths ranging from 3 to 54 μm. The prelaunch clear-sky retrieval algorithm, evaluated with simulated test data, indicates that PREFIRE measurements will be valuable for retrieving atmospheric water vapor and temperature profiles. Far infrared measurements provide unique retrieval information, indicated by the high ranking of select FIR channels as primary contributors to the total degrees of freedom for signal (DFS). In utilizing all the PREFIRE channels, the average total DFS of 4 test regions ranges from 1.90 to 4.71. The information content increases with higher column water vapor and in the presence of near-surface temperature inversions. Using the DFS profiles for guidance, the retrieval concentrates information into 7 distinct layers to reduce the retrieval uncertainty per layer. Sensitivity tests indicate forward model error due to surface emissivity uncertainty results in about a 9% increase in column water vapor uncertainty. The clear-sky retrieval is sensitive to the presence of undetected ice clouds, especially those with optical depths larger than 0.2. Hence, in addition to a separate PREFIRE cloud mask, optimal estimation retrieval metrics are explored as possible indicators of cloudy scenes.

KEYWORDS: Atmosphere; Antarctica; Arctic; Satellite observations

1. Introduction

The far infrared (FIR; defined here as 15–50 μm) plays an important role in establishing the energy balance of the Earth system. Differential solar heating between low and high latitudes leads to colder polar temperatures, driving atmospheric and oceanic energy transport from warm to cold regions (Serreze et al. 2007). Since the wavelength of peak emission is inversely proportional to temperature, cold polar regions emit as much as 55%–65% of the infrared thermal energy in the FIR (L'Ecuyer et al. 2021). Thus, it is especially important to have FIR coverage for characterization of atmospheric/surface energy exchange in polar regions.

The ability of surface emitted infrared radiation to escape to space is determined by the atmospheric transparency. The most transparent atmospheric window for thermal emission is a broad spectral interval (approximately 8–14 μm) within the midinfrared (MIR; 5–15 μm) part of the electromagnetic spectrum. The peak transparency of the MIR window decreases with increasing water vapor, but large parts of this window have high (>80%) transmission in all Earth climate conditions. Another region of partial transparency, often referred to as a "dirty" window, exists in the FIR part of the electromagnetic spectrum from 17 to 24.4 μm where some microwindows exhibit high transmission over small spectral intervals (Rathke et al. 2002). This FIR window is not fully transparent and its opacity depends strongly on the amount of water vapor present in the atmosphere, which varies significantly both spatially and temporally (Chen and Liu 2016). In high water vapor amounts in the tropics the FIR window may be fully "closed," and opaque to upwelling thermal radiation, but in low water vapor amounts that occur in the polar regions the transmission can be significant (Feldman et al. 2014). Hence, the FIR atmospheric window plays a critical role in the regulation of global temperatures by cooling to space in the cold and dry polar regions. The strong sensitivity of outgoing FIR emission to atmospheric water vapor is also the basis for FIR water vapor retrievals.

Direct measurements of water vapor, critical for predicting weather and understanding the climate system, have been made for decades across the polar regions by radiosondes (Durre et al. 2006). In addition, ground-based microwave radiometers provide estimates of total column water vapor (CWV) using accurate retrieval techniques (Turner et al. 2007). Imaging of water vapor from geostationary satellites provides enhanced spatial and temporal coverage (Schmit et al. 2018). Vertical distributions of moisture can be obtained from satellite-based infrared sounders in low-Earth orbit (Menzel et al. 2018) providing global coverage of water vapor profiles from missions such as AIRS (Maddy and Barnet 2008), IASI (Hilton et al. 2012), and CrIS (Nalli et al. 2013). All such instruments currently utilize the MIR; however, Merrelli and Turner (2012) show that utilizing upwelling spectra that includes the FIR enhances the degrees of freedom for signal and increases the information content available for temperature and water vapor profiling retrievals. Other studies support the idea that the FIR is useful for not only the lower troposphere

Corresponding author: Nathaniel B. Miller, nbmiller@wisc.edu

DOI: 10.1175/JTECH-D-22-0128.1

(Turner and Mlawer 2010) but also the upper troposphere and lower stratosphere (Shahabadi and Huang 2014; Palchetti et al. 2015; Warwick et al. 2022). Planned implementation of FIR sensors on upcoming satellite missions will, therefore, be beneficial not just for measuring the complete emission spectrum, but also providing unique sensitivity applicable to temperature and water vapor retrievals especially in cold, dry regions.

The first spaceborne spectral FIR measurements were made using the Infrared Interferometer Sounder instrument on the *Nimbus-3* (Hanel et al. 1970) and *Nimbus-4* (Hanel et al. 1971) at wavelengths extending to 25 μm. Over 50 years later the Polar Radiant Energy in the Far Infrared Experiment (PREFIRE; L'Ecuyer et al. 2021) will collect spectral measurements in both the mid- and far IR. In fact, PREFIRE will be the first satellite mission to sample the FIR spectra since the Fourier spectrometer on *Meteor-25* and *Meteor-28* (Kempe et al. 1980), which launched in 1976 and 1977 providing spectra radiance from 6 to 25 μm. With a 1.3° cross-track field of view PREFIRE will improve spatial resolution by a factor of 2–6 compared to the previous FIR spaceborne measurements (Kempe et al. 1980), significantly increasing the likelihood of observing clear-sky scenes. In addition, PREFIRE will have moderate spectral resolution output (with spectral sampling at approximately 0.84 μm), paving the way for future missions such as ESA's Far-infrared Outgoing Radiation Understanding and Monitoring (FORUM; Palchetti et al. 2020), which will measure the FIR at high spectral resolution.

PREFIRE will collect infrared spectra ranging from 3 to 54 μm for at least one year using a Thermal Infrared Spectrometer (TIRS). The TIRS instrument is an imaging spectrometer small enough to fly aboard a relatively low cost CubeSat spacecraft, with approximate dimensions of 300 mm by 200 mm by 100 mm. A second TIRS instrument with similar specifications will orbit on a separate CubeSat spacecraft with a distinct equatorial crossing time. Launching two CubeSats will provide time-differenced measurements in the poles to capture processes that occur on subdiurnal time scales. These measurements will be used not only for water vapor retrievals, but also for detecting cloud presence, discerning cloud phase, and retrieving surface emissivity. Reliable water vapor retrievals will be used as input into other retrievals, including surface emissivity, effectively enhancing prior knowledge of the atmospheric state and the resultant atmospheric greenhouse effect.

To provide immediate science and data products after launch and in the absence of existing global FIR spectral measurements, simulations must be performed prelaunch to gauge the accuracy and information content of retrieved variables from TIRS measurements. An optimal estimation framework (Rodgers 1976) is utilized to retrieve atmospheric profiles of temperature and specific humidity as well as surface temperature and integrated CWV. This technique reports an associated uncertainty for each retrieval and is useful for estimating the degrees of freedom for signal (DFS) that is indicative of the amount of distinct information contained in the measurements relative to an assumed a priori state. In this paper we investigate the information content of the various TIRS channels and characterize the clear-sky retrieval uncertainty using simulated observations from reanalyses at three different polar regions that include the Greenland ice sheet, Arctic Ocean, and Antarctica. PREFIRE will collect global measurements; thus, we also investigate a fourth region in the tropics to evaluate performance in humid environments. Forward model error due to the influence of the error in surface emissivity and undetected clouds are also characterized. Ultimately, these simulated results will be the foundation upon which to derive atmospheric water vapor profiles from TIRS observations after PREFIRE launches.

2. TIRS instrument

TIRS is an Offner-style imaging spectrometer, built to measure 8, 64-channel spectra (from 3 to 54 μm) simultaneously, using a 64 $\times$ 8 element custom detector array. Instrument constraints will have channel gaps at approximately 7, 15, and 30 μm, resulting in 54 unique useable channels, spaced approximately every 0.84 μm, with modeled spectral response functions (SRFs) shown in Fig. 1b. Due to acceptable risks for low-cost, rapid deployment, some detector elements on the operational TIRS instruments may be unusable resulting in fewer channels for each of the cross-track spectra, but the analysis that follows assumes complete spectra for these initial simulations. Although the orbiting altitude of the PREFIRE satellite will determine the precise spatial resolution and coverage of the TIRS measurements, it is estimated that one scene will have a spatial footprint of approximately 12 to 15 km, with a distance of 250 km separating the first and eighth scene in the cross-track direction.

A modeled spectrum, from a subarctic winter atmospheric profile (McClatchey et al. 1972), illustrates the radiances at high spectral resolution (Fig. 1a). Convolving the spectrum in Fig. 1a with the SRFs in Fig. 1b results in an estimated TIRS measurement in Fig. 1c. The noise equivalent delta radiance (NEDR) provides an estimate of the sensor performance for each of the 54 channels (Fig. 1d). The ratio of the radiance to NEDR determines the signal-to-noise ratio (SNR) shown in Fig. 1e. It is evident that the largest SNR regions are from 8 to 28 μm and SNR is expected to be low at wavelengths greater than 30 μm.

3. Optimal estimation retrieval algorithm

An optimal estimation framework retrieves temperature and water vapor profiles using the different sources as listed in Table 1. Auxiliary meteorological analysis data are used to determine the a priori mean of the state variables and provides necessary inputs for running the forward model. The a priori covariance of the retrieved variables, described in section 3c, is utilized as a static input. Calibrated spectral radiances from the TIRS instrument provide unique information to the atmospheric retrieval and are also critical input for the cloud mask and the surface emissivity retrieval. In the PREFIRE processing system, any time a distinct cloud mask deems a specific footprint a clear-sky scene then the atmospheric

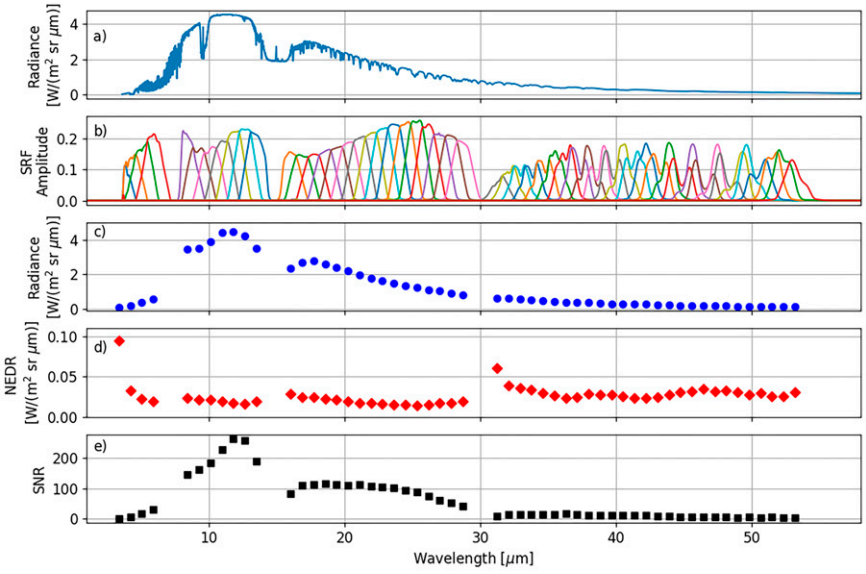

FIG. 1. (a) Modeled spectral radiance using the subarctic winter profile (McClatchey et al. 1972), (b) modeled spectral response functions (SRFs) of the 54 TIRS channels, (c) TIRS channel radiances after convolution of SRFs from (b) with the high resolution spectrum in (a), (d) noise-equivalent delta radiance (NEDR), and (e) the resultant signal-to-noise ratio.

retrieval is performed using the surface emissivity retrieval as input.

a. Overview and framework

The optimal estimation (OE) approach developed by Rodgers (2000), which has become widely used in retrieving atmospheric properties (Maahn et al. 2020; Turner and Löhnert 2014), is the basis for the physical retrieval used in this paper. One of its major advantages is that the OE method reports an uncertainty for each retrieved parameter as constrained by the uncertainties in the measurements and prior information. In general, the goal of a retrieval is to derive an estimate for an unknown state vector $\mathbf{x}$ from a known measurement vector $\mathbf{y}$. These two vectors are related using a forward model $\mathscr{F}$:

$$y = \mathscr{F}(\mathbf{x}) + \epsilon, \tag{1}$$

where ϵ represents the measurement noise. In this study we relate the state variables to the TIRS spectra using the forward model discussed in section 3b.

The state vector is initialized using an a priori estimate, before the algorithm iterates the state vector value (a standard nonlinear cost-function minimization) by calculating the forward modeled spectral radiance and Jacobians at each step. The state variables include atmospheric profiles of temperature and specific humidity Q, and surface temperature. The humidity state variables are equal to the natural logarithm of Q. Transforming to the logarithmic state space improves the numerical stability for the water vapor profile, since the values of Q span multiple orders of magnitude through the vertical profile. The logarithm also avoids numerical issues that could arise from state updates that produce negative specific humidity in the linear space. Furthermore, in most real atmospheric data, the logarithm of Q more closely resembles a normal distribution than Q itself. Since one of the fundamental assumptions of OE is that deviations from the prior mean are normally distributed, transforming Q in this manner helps ensure the data are more suitable for the OE method (Maahn et al. 2020). Last, the retrieval calculates the total CWV and the associated uncertainty by integrating the profile of the retrieved specific humidity.

TABLE 1. Various inputs into the Atmospheric OE retrieval algorithm (2B-ATM).

Name	Description
Aux-Met	Auxiliary meteorological analysis data
Static information	A priori covariance matrix
L1B-RAD	Measured TIRS spectral radiance
2B-MSK	Cloud mask for determining clear conditions
2B-SFC	Retrieved surface spectral emissivity

b. Forward model

The radiative transfer model that is used to relate the state variables to the measurements is the Principal Component–based Radiative Transfer Model, version 3.4 (PCRTM; Liu et al. 2006). The PCRTM operates on 101 fixed vertical pressure levels. Inputs include profiles of temperature, specific humidity, ozone, CO_2, CH_4, CO, and N_2O. The surface is characterized by pressure, temperature, and emissivity. The PCRTM uses an instrument model for a thermal infrared spectrometer with continuous spectral coverage from 50 to 2760 cm^{-1} (approximately 3.6 to 200.0 μm in wavelength) with 0.5 cm^{-1} wavenumber sampling. The surface emissivity

input is gridded across 740 wavenumbers and includes the FIR. This high resolution spectrum is convolved with the TIRS spectral response functions, thus modeling the TIRS spectra.

c. *A priori data*

The OE algorithm uses an initial starting point, or a priori value, before the TIRS measurements are factored in. The a priori mean values are derived from the analysis fields and interpolated to the location and time of the TIRS observations. A probability distribution in the form of a covariance matrix represents the errors in the analysis fields compared to the true state. These errors include inherent error in the analysis model, error due to spatial and temporal interpolation, and any unresolved spatial features due to limited resolution of the analysis model. Accurate estimates of the covariance are difficult since it requires large datasets of independent known truth profiles. An estimate of the temporal interpolation error covariance can be computed by comparing the analysis profiles to the averaged values of the +6- and −6-h time steps. This estimate will contain realistic vertical error correlations in the atmospheric profile, assuming the analysis data accurately represent atmospheric transport.

Initially, the first guess into the OE retrieval is from the National Aeronautics and Space Administration (NASA) Global Modeling and Assimilation Office (GMAO) GEOS5 FP-IT analysis data (Lucchesi 2015); thus, GOES FP-IT data are used to compute the a priori covariance matrices. For the temperature and water vapor profiles the analysis data have a time step of 3 h; hence, using the interpolation of the ±6-h time steps, as described above, will provide a conservative estimate for the error to account for unknown factors. Investigating the variance over a wide range of latitudes, longitudes, and seasons it is found that the covariance from the analysis model has very little seasonal or longitudinal dependence, and only small latitudinal dependence mostly due to the change of the tropopause height. The variance in the troposphere (below approximately 100 hPa) is approximately $(1.0\ \mathrm{K})^2$ for temperature and $(0.2)^2$–$(0.6)^2$ for $\log(Q)$. The vertical correlation scales are approximately 100–200 hPa for both temperature and $\log(Q)$ in the troposphere. Above the troposphere, the variance is relatively more restricted.

Our final a priori covariance for temperature, guided by the analysis of GEOS FP-IT analysis described above, uses an autoregressive correlation model (Lerner et al. 2002) with a correlation length scale for T and $\ln(Q)$ of 200 hPa in the lower atmosphere and 100 hPa in the upper atmosphere. These correlation length scale estimates are similar to the values reported by Errico and Privé (2014), for an analysis of GMAO profiles. The variances are set to be moderately conservative in the sense that the retrieval should not be too closely constrained to the prior, so the tropospheric variances are set to $(2.0\ \mathrm{K})^2$ for temperature and $(0.6)^2$ for $\log(Q)$. The primary focus of this retrieval is on temperature and Q in the troposphere; thus, in the stratosphere the variances are reduced to $(0.5\ \mathrm{K})^2$ and $(0.3)^2$. The surface temperature a priori variance is set to $(2.0\ \mathrm{K})^2$ in order to match the variance for the near-surface atmospheric temperature. Figure 2 shows the $\ln(Q)$ correlation matrix and variance at all 101 PCRTM pressure levels, which has the same structure as the temperature correlation matrix (not shown). The operational algorithm will not have any estimate of the atmospheric state other than the NWP analysis fields. Therefore, the prior mean will also be used as the first guess to start the iterative OE algorithm.

4. Test dataset

Three polar regions are investigated to establish retrieval performance. The first region is in the relatively warm (surface temperatures ranging from 247 to 285 K) Arctic Ocean, east of Greenland in the Greenland Sea from 70° to 80°N and from 5°W to 5°E. The second region, from 70° to 80°N and from 45° to 35°W, is in central Greenland which has inherently high surface elevation (surface temperatures ranging from 219 to 271 K). The third region samples Antarctica for all longitudes with a latitude range from 80° to 85°S, providing sample test data over a variety of elevations across the Antarctic ice sheet (surface temperatures ranging from 200 to 275 K). The final region is in the much warmer (surface temperatures ranging from 298 to 303 K) tropical Pacific Ocean, northeast of Papua New Guinea on the equator, spanning 5°S to 5°N and 160°–170°E. This region provides example atmospheric profiles representative of high amounts of column water vapor that will be observed in the global PREFIRE dataset.

Atmospheric profiles of temperature, water vapor, and ozone from ERA5 (Hersbach et al. 2020) are randomly sampled from 2016 resulting in 8000 reanalysis test profiles for each region. The temperature and water vapor fields are the primary atmospheric inputs that will affect the TIRS radiances. The terrain following 137 model pressure level ERA5 data is interpolated to the fixed PCRTM 101 model levels and the lowest model level is used as an estimate of surface skin temperature. The surface pressure from ERA5 is also used as an input into PCRTM. In this study CO and N_2O PCRTM inputs are from the standard subarctic winter values as given by McClatchey et al. (1972). In addition, fixed values for CO_2 and CH_4 of 400 and 1.8 ppm, respectively, are used as PCRTM input.

Realistic surface emissivity values are estimated using the reported emissivities of four surface types in Huang et al. (2016). For the tropics region the surface emissivity is always that of pure water. For the Greenland and Antarctica regions the surface emissivity is a randomly selected mixture of snow types, which include fine, medium, and coarse snow as defined in Huang et al. (2016). For the Arctic Ocean region, if the surface temperature is above 277 K then the surface type is assumed to be pure water and if the surface temperature is below 269 K the surface types are randomly selected with possible values of fine, medium or coarse snow. If the surface temperature is between the upper and lower threshold, then the surface emissivity is randomly selected mixtures of two of the four aforementioned surface types.

5. Degrees of freedom for signal

To quantify the information content of the temperature and water vapor profiles we use the metric of DFS as defined

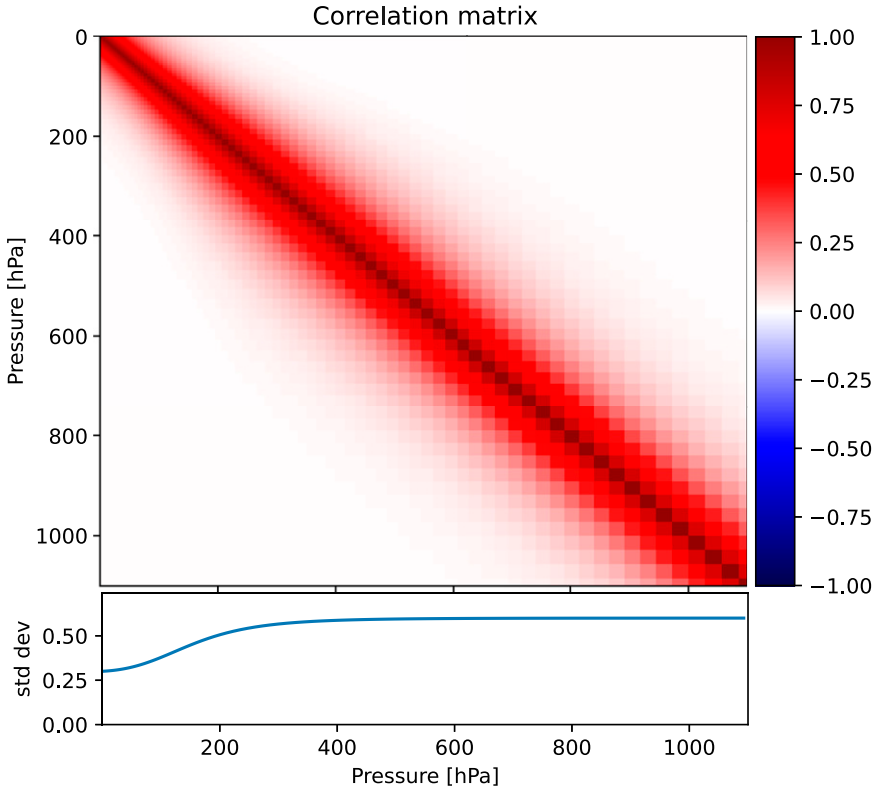

FIG. 2. (top) Correlation matrix of log(Q) for the 101 PCRTM pressure levels. (bottom) The standard deviation at each pressure level.

in Rodgers (2000). The total DFS is the trace of the averaging kernel (A) and the DFS profile is the diagonal of A. The averaging kernel is given by

$$A = (\mathbf{K}^{\mathrm{T}}\mathbf{S}_e^{-1}\mathbf{K} + \mathbf{S}_a^{-1})^{-1}\mathbf{K}^{\mathrm{T}}\mathbf{S}_e^{-1}\mathbf{K},$$

where the Jacobian $\mathbf{K}$ is calculated from PCRTM, the a priori covariance $\mathbf{S}_a$ is described in section 3c, and the error covariance $\mathbf{S}_e$ is equal to the squared noise equivalent radiance (NEDR) with no correlated error between channels. Figure 3 shows example temperature and log(Q) Jacobians for the TIRS channels from a subarctic winter profile, which has a temperature and moisture inversion below 850 hPa. It is evident that there is significant sensitivity in the FIR to temperature and water vapor at various levels in the atmosphere, including primarily upper atmosphere levels for wavelengths greater than 30 μm.

a. *Total DFS*

Various factors influence atmospheric moisture information content, including CWV and surface properties such as

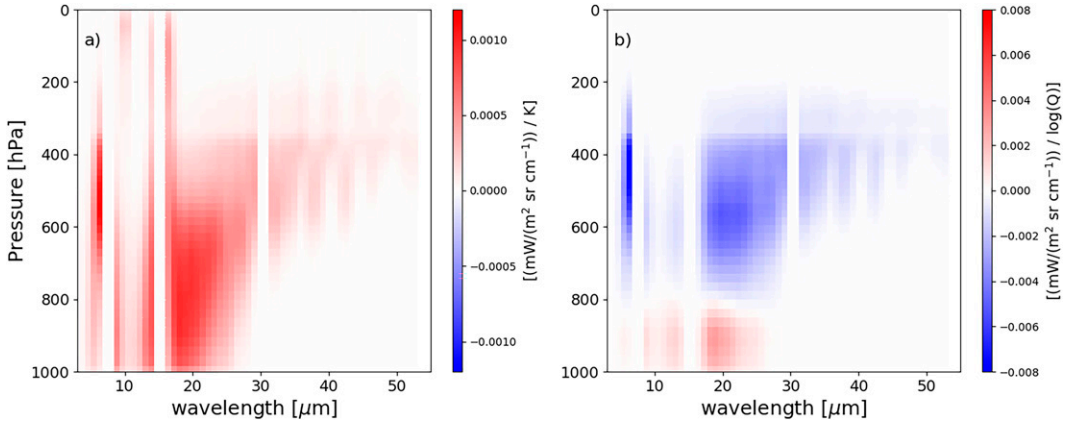

FIG. 3. Jacobians of (a) temperature and (b) log(Q) calculated from standard subarctic winter profiles.

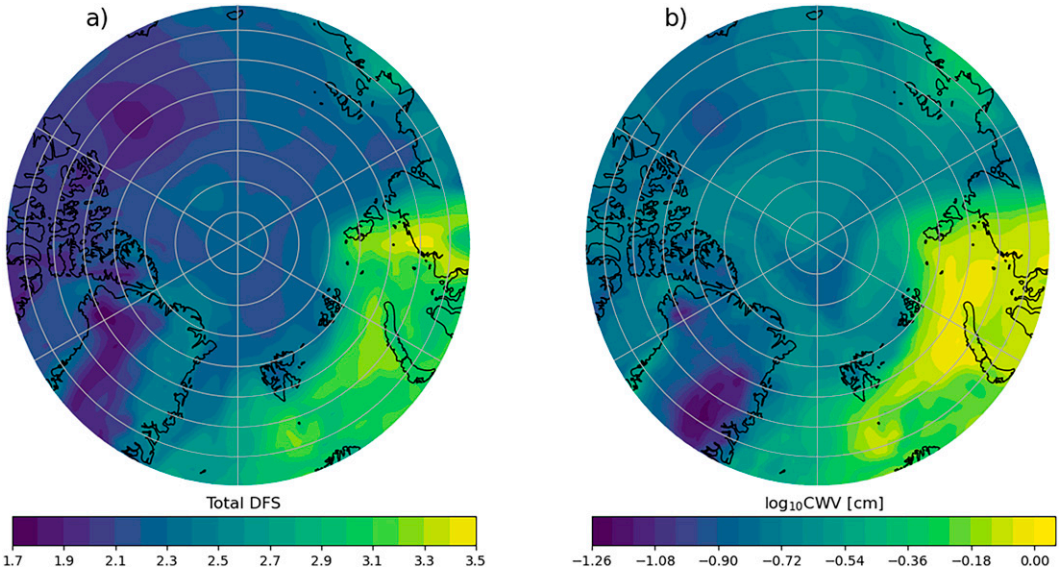

FIG. 4. ERA5 derived (a) total degrees of freedom for signal (DFS) and (b) column water vapor (CWV) at 0000 UTC 1 Apr 2016 across the Arctic (70°–90°N).

elevation, emissivity, and skin temperature contrast with near-surface air temperature (Di et al. 2016). Regional distribution of the total DFS across the Arctic is depicted at 0000 UTC 1 April 2016 using ERA5 data (Fig. 4). Although the TIRS instrument is not an imager, Fig. 4 provides a regional depiction of the information content available at this specific time. The total DFS spatial distribution is very similar to that of the $\log_{10}$CWV, with some small-scale differences, suggesting atmospheric profiles with relatively large CWV have enhanced total DFS.

The total DFS for the joint temperature and water vapor retrieval is highly dependent on the amount of CWV present. Investigating the total DFS for all test regions (Fig. 5) shows that an increase in CWV corresponds to an increase in DFS. The profiles with the smallest CWV profiles have DFS values near 1 and the tropics region (indicated by the separate cluster of large CWV values in Fig. 5) have DFS values as large as 5. The average total DFS for the Arctic Ocean, Greenland, Antarctica, and tropics regions are 3.11, 2.15, 1.90, and 4.71, respectively.

Temperature inversions at the surface are prevalent in the cold and dry conditions at the poles (Zhang et al. 2011). Here we simply define the temperature inversions strength as the maximum temperature in the boundary layer minus the surface temperature. For small CWV conditions the presence and strength of temperature inversions increase the DFS at a given CWV value (Fig. 6), thus indicating a secondary influence on total DFS to the primary effect of CWV in enhancing the total DFS (Fig. 5).

b. Channel rank

The relative importance of TIRS channels to the DFS can be assessed by sequentially determining which channels contribute the most information content to the retrieval. This channel selection works by first computing the DFS for each individual channel, and selecting the channel with the maximum DFS. For each successive selection, the DFS is computed for each unselected channel, given the fixed list of already selected channels, and the channel that produces the

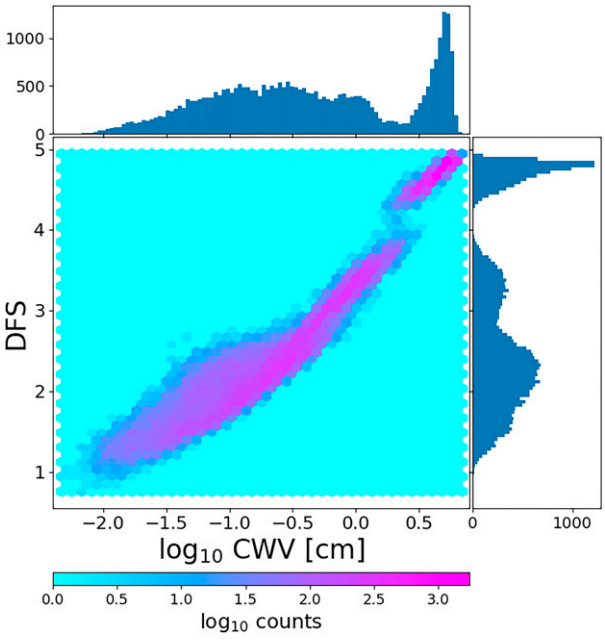

FIG. 5. Total DFS of the temperature and specific humidity retrievals as sampled from all four test regions. The total DFS is shown as a function of $\log_{10}$ of the CWV. The color bar indicates $\log_{10}$ of the number of counts. The histograms along the x and y axes indicate the one-dimensional distribution of $\log_{10}$CWV and DFS, respectively.

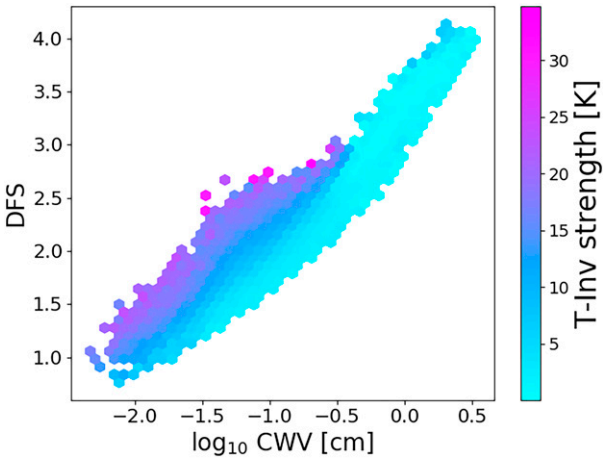

FIG. 6. DFS as a function of $\log_{10}$CWV, similar to Fig. 5, but considering only the three polar test regions in the Arctic Ocean, Greenland, and Antarctica. The color bar indicates the average strength of a temperature inversion (T-Inv) at a given DFS and CWV bin.

largest DFS increase is selected. This process is repeated for all available TIRS channels, which results in a channel selection ordered by DFS, similar to information content studies of cloud properties (L'Ecuyer et al. 2006; Chang et al. 2017). Channel ranking is repeated for each of the 8000 profiles in the Arctic Ocean, and channel 7 (at 5.9 μm) is ranked first in 19.3% of cases, channel 15 (at 12.7 μm) in 17.9% of cases, channel 22 (at 18.6 μm) in 27.5% of cases, channel 25 (at 21.1 μm) in 26.9% of cases, and 6 other channels with occurrences below 4%. Figure 7 illustrates the channel rank of all 54 active channels as a fractional occurrence, highlighting the importance of using the FIR channels in green. The FIR channels from 31.2 to 53.2 μm are generally ranked lower than all the other channels, excluding channels 4–5, indicating less information content due, in part, to high NEDR values.

c. *Vertical distribution of information*

The diagonal of the averaging kernel matrix shows how the DFS are distributed across the 101 pressure levels. The density of occurrence for the temperature profiles (Fig. 8a) and the Q profiles (Fig. 8c) shows similar patterns, with low information in the upper atmosphere (pressure $<$ 200 hPa), and evenly distributed information through the troposphere and a slight increase near the surface. To reduce the retrieval output size, to distribute the information approximately equally across layers, and retain independent layer information, the full resolution PCRTM levels are combined into 7 distinct layers. The bounding pressure levels for the 7 layers are set to be 0.005, 156, 307, 433, 565, 718, 892, and 1100 hPa. These layers are similar to those used in the AIRS retrievals (Maddy and Barnet 2008; Susskind et al. 2003) but with a smaller number of coarse layers. The last bounding pressure level is actually set to the surface pressure for a given profile. Consequently, the final bounding value is less than 1100 hPa and for high elevation terrain the low values of surface pressure may truncate the number of filled atmospheric layers to include less than 7 temperature and specific humidity values. These layer values are the mean of the high vertical resolution level group, and the posterior covariance and averaging kernel matrix are recomputed using the block averaged prior covariance and Jacobian. Figure 8 shows the increase in DFS for the combined layer profiles in Figs. 8b and 8d, compared to the full vertical resolution profiles Figs. 8a and 8c.

6. OE retrieval tests

To test the performance of the PREFIRE atmospheric OE retrieval, we conduct synthetic retrievals using simulated TIRS spectra from each of the four regional test datasets

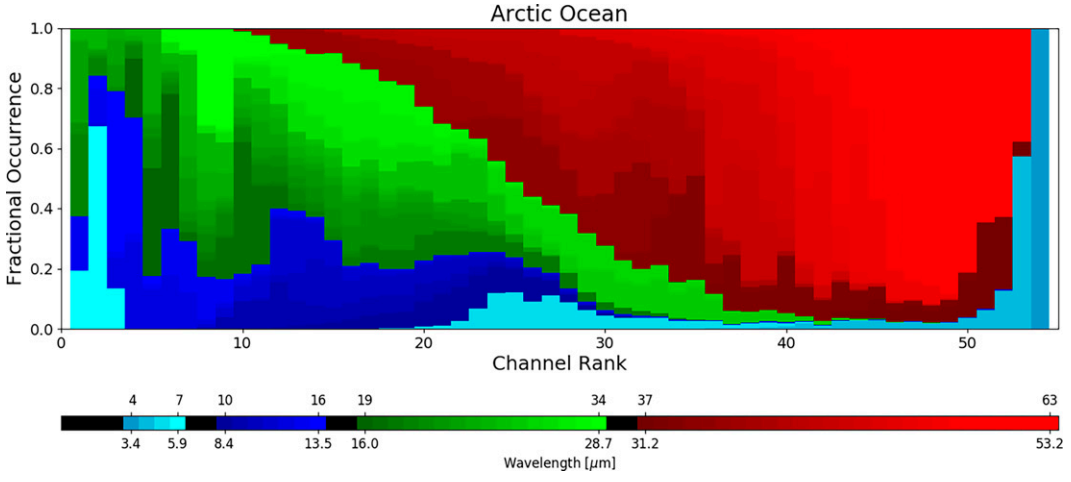

FIG. 7. Fractional occurrence of each of the 63 channels (top numbers on the color bar) ranked in order from the highest to lowest DFS contributions for the Arctic Ocean region. Masked channels are shown in black in the color bar, resulting in 54 active channels. The numbers below the color bar indicate the central wavelength (μm) of the 63 channels.

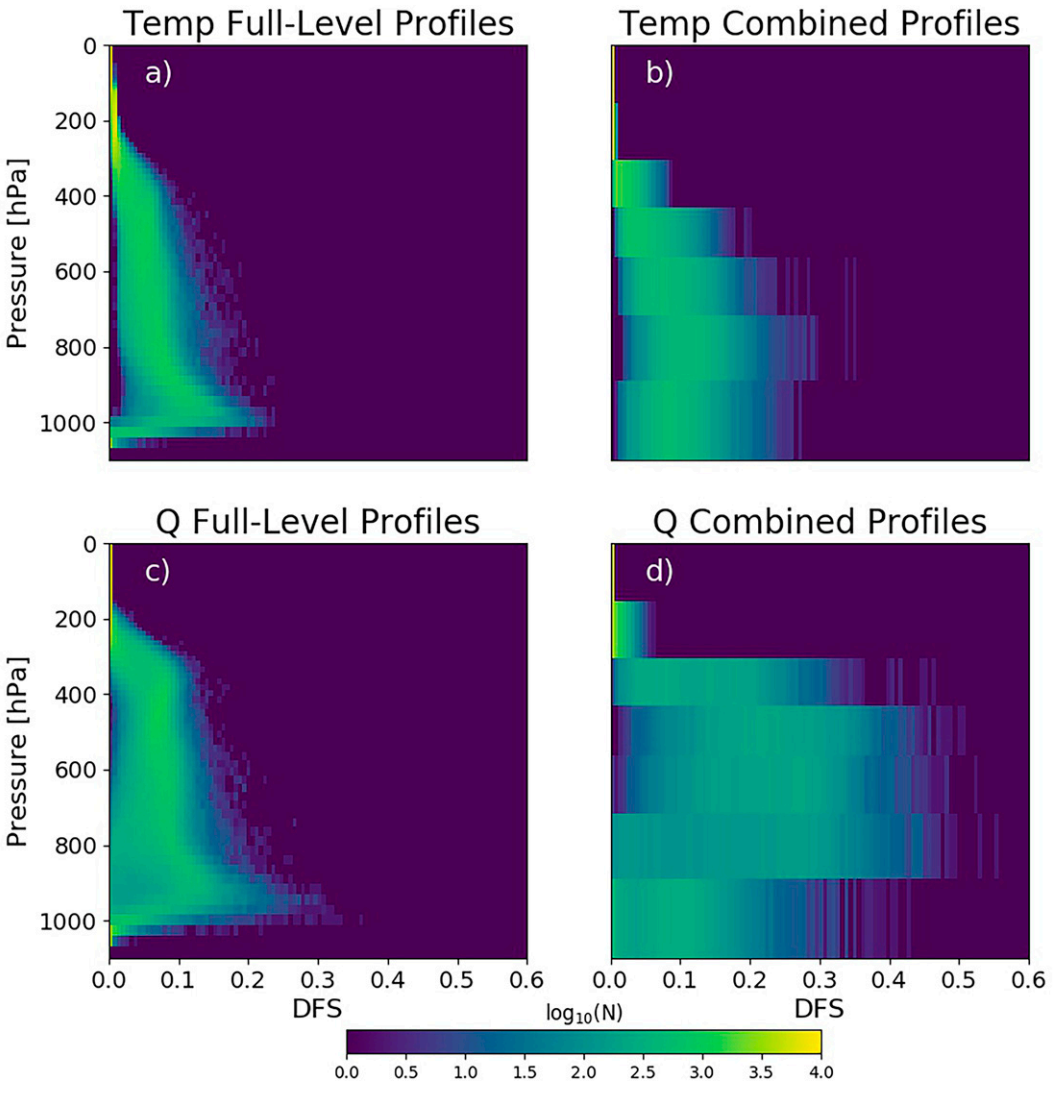

FIG. 8. Density of occurrence for DFS profiles. The full 101 pressure levels are shown for (a) temperature and (c) specific humidity Q. The combined layer DFS values are shown for (b) temperature and (d) specific humidity.

detailed in section 4. Realistic sensor noise is simulated using the NEDR values and added to the modeled TIRS radiances described in section 3b. In addition, the "truth" values of the temperature profiles, log(Q) profiles, and surface temperature are perturbed according to the prior dataset, with similar level-to-level covariance and a priori standard deviation values of 2.0 K, 0.6 log(g kg^{-1}) (which is about 80% of the Q value), and 2.0 K, respectively. These perturbed values are used as the first guess and prior for the OE retrieval, following the retrieval design described in section 3c. The vertical resolution of the atmospheric OE retrieval can be output on the native PCRTM 101 levels or in the 7-layer combined output, described in section 5c.

a. *Sample retrievals*

An example retrieval in the Arctic Ocean region illustrates results for the temperature and specific humidity profiles (Fig. 9). The simulation framework uses the perturbed profile as the prior and first guess and then the algorithm converges to the retrieved value. The shaded envelope around the retrieved value represents the reported 1-sigma uncertainty from the OE retrieval. If the random perturbation that defines the simulated prior is less than a 1-sigma deviation from the truth value, then the uncertainty envelope will contain the truth profile and the residual value at that level would be less than the reported uncertainty. Furthermore, since the TIRS measurements provide enhanced information content, it is expected that the standard deviation of the residuals will be less than the a priori standard deviation values for a sufficient sample size.

b. *Clear-sky performance characterization*

Differences between the retrieved values and the truth values indicate whether the retrieval is relatively unbiased,

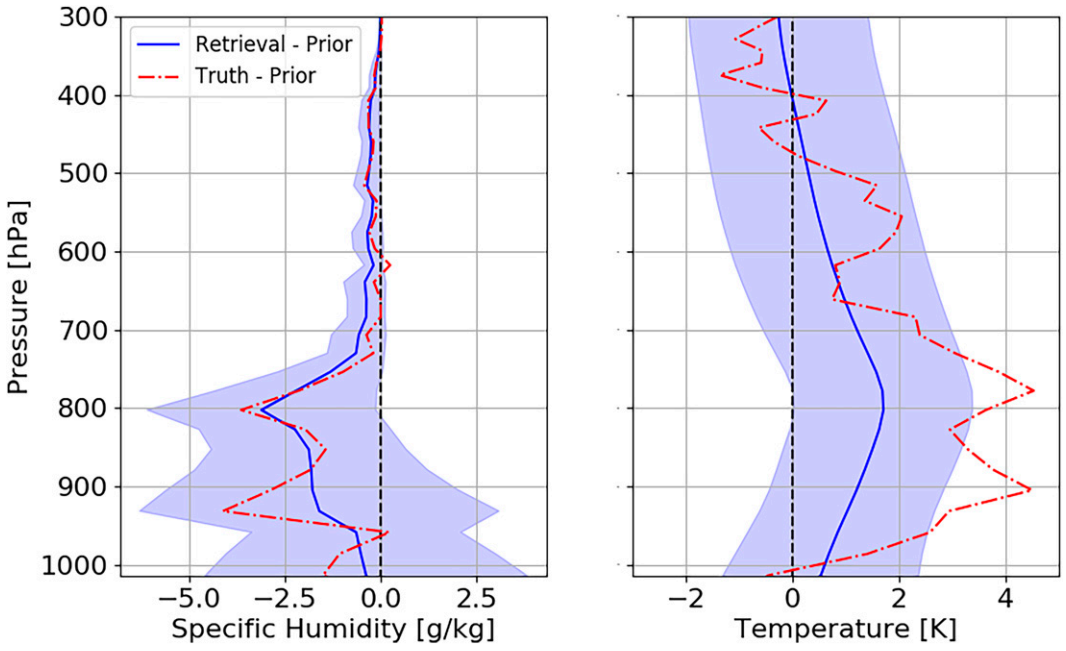

FIG. 9. Sample retrievals of Q and temperature for a test case in the Arctic Ocean region. The red dashed–dotted line is the "truth" − prior profile, and the blue solid line is the retrieved − prior profile. The shaded envelope around the retrieved − prior profile represents the reported uncertainty of the retrieval.

enhancing the accuracy from the prior, and reporting representative uncertainty values. Here the residuals are defined as the retrieved − "truth" values. The temperature profiles biases are very small, with an average bias of 0.0026 K throughout the 101-level profile and across all four regions. The maximum bias for the 7-layer profile output is 0.092 K, occurring in the Arctic Ocean region. The largest bias in surface temperature occurs in the tropics regions with a bias value of −0.16 K. If the OE retrieval is properly constructed, then the simulated biases will be small (as reported here),

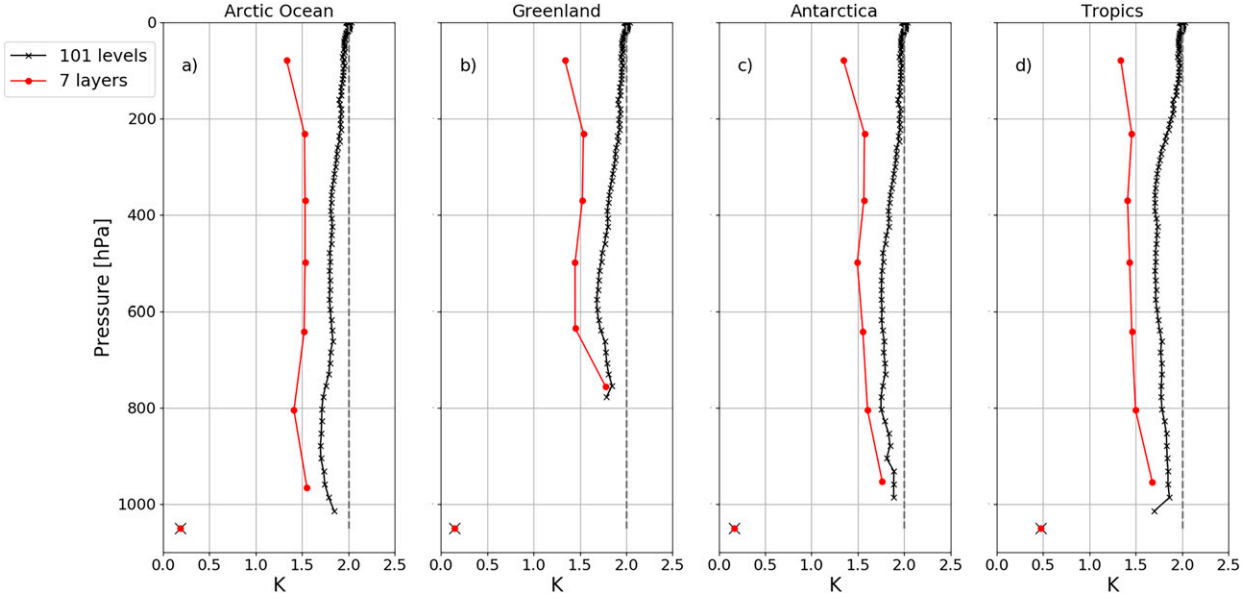

FIG. 10. Standard deviation of the temperature residuals (retrieved − "truth") for the 101-level (black) and 7-layer (red) output for the (a) Arctic Ocean, (b) Greenland, (c) Antarctica, and (d) tropics region. The standard deviation of the surface temperature residuals is shown by the markers located at 1050 hPa. The dashed gray line at 2.0 K represents the size of the perturbations, which are equal to the prior uncertainty through the troposphere.

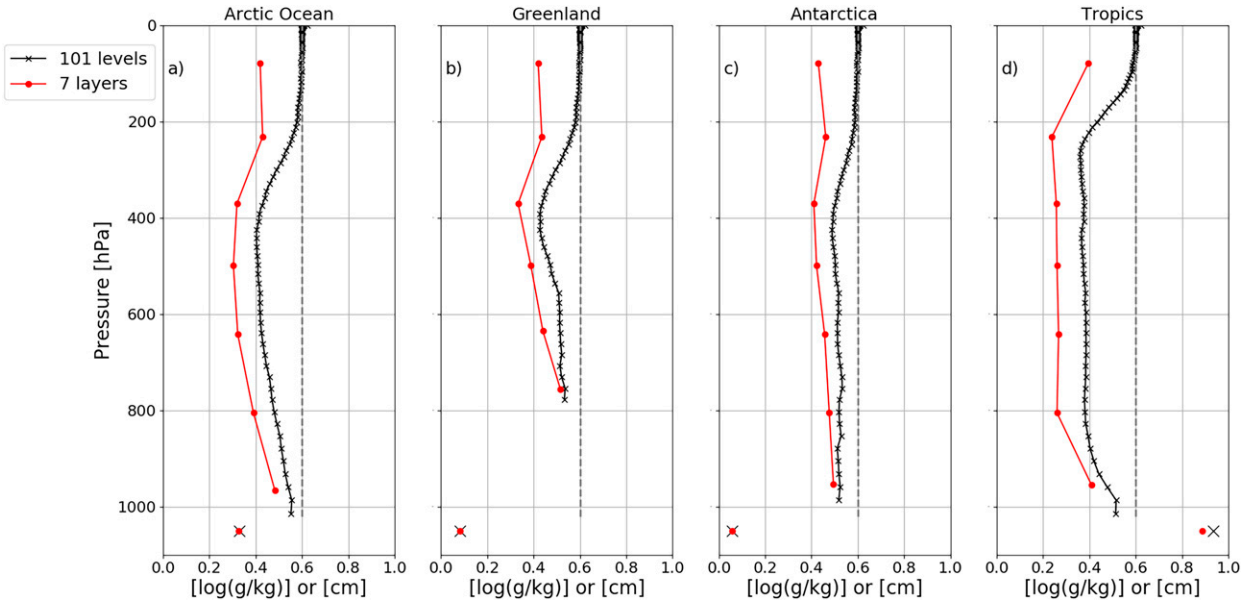

FIG. 11. Standard deviation of the Q residuals (retrieved − "truth") [log(g kg^{-1})] for the 101-level (black) and 7-layer (red) output for the (a) Arctic Ocean, (b) Greenland, (c) Antarctica, and (d) tropics region. The standard deviation of the CWV residuals (cm) is shown by the markers located at 1050 hPa. The dashed gray line at 0.6 represents the size of the perturbations, which are equal to the prior uncertainty through the troposphere.

although these simulated values do not account for on-orbit biases in the measured radiances that lead to larger bias in the atmospheric retrievals.

The standard deviation of the residuals for all 4 regions are shown in Fig. 10. Consistent with the DFS profile analysis, there is a reduction in variability of the residuals from the 2 K perturbation of the first guess, where the reduction is greatest near 800–900 hPa for the Arctic Ocean region and minimal reduction in the upper atmosphere (pressure $<$ 100 hPa). For the 7-layer retrieval output the reduction in variation of the residuals is reduced further with values around 1.5 K throughout the atmospheric profile, indicating that the information content is enhanced by averaging out some of the random noise in the high-resolution profile. The individual markers at 1050 hPa indicate the standard deviation of the residuals for surface temperature which are reduced substantially from the initial perturbations of 2 K. As a final metric, the standard deviation of the residuals divided by the reported uncertainty is found to be approximately 1 throughout the profile, indicating the reported uncertainty of the OE retrieval is accurate.

Retrieval statistics of the moisture profiles reveal similar results to the temperature profiles. The largest bias value [−0.12 log(g kg^{-1})] of the 7-layer output is found in the tropics region, while the polar regions all have values less than 0.086 log(g kg^{-1}). Figure 11 indicates that for the full 101 level output there is a very small reduction in the variance [initially 0.6 log(g kg^{-1})] of the residuals above 200 hPa. The standard deviation of the residual does reduce to 0.4 log(g kg^{-1}) between ~400 and 650 hPa and is reduced at all levels for the 7-layer retrieval output. As found with the temperature results, unity values of the scaled Q residuals are indicative that the reported uncertainty is representative of the actual error in Q.

The retrieved integrated water vapor amount is useful for input into the surface emissivity algorithm because the transparency of the atmosphere due a lack of water vapor allows for the possibility of retrieved surface emissivity from direct measurements. The markers at 1050 hPa in Fig. 11 depict the standard deviation of CWV in units of cm. Those values and other CWV statistics are summarized in Table 2 for each of the 4 test regions. CWV bias values are small and the ratio of the standard deviation of the residuals to the mean CWV are higher for drier regions. These statistics support the total DFS results in section 5a, indicating that the regions with higher DFS (that also have higher CWV values) will ultimately have lower percent uncertainty compared to a region with low DFS and CWV.

TABLE 2. Column water vapor retrieval statistics for the 4 test regions.

	Arctic Ocean	Greenland	Antarctica	Tropics
Bias (cm)	0.03	0.01	0.01	−0.16
Std dev of residuals (cm)	0.33	0.08	0.06	0.89
Mean (cm)	0.88	0.20	0.11	4.92
Std dev of residuals/mean (%)	37.3	40.5	50.6	18.0

c. Error considerations

The two primary inputs that are from other PREFIRE algorithms are a cloud mask and surface emissivity values; hence, it is beneficial to estimate forward model error due to uncertainty of these inputs. PCRTM is modeling clear-sky conditions; thus, if any clouds are unaccounted for and the cloud mask deems the scene "clear sky" this will lead to error in the radiances. Xie et al. (2022) describe surface emissivity retrieval that will be used as input to the atmospheric retrieval; thus, the reported spectral uncertainties of surface emissivity are used to estimate the forward model error and the influence on the atmospheric retrieval accuracy.

1) Influence of surface emissivity uncertainty

To investigate the impact of the surface emissivity error on the atmospheric retrievals, statistics for the Arctic Ocean region are calculated using perturbed surface emissivity and compared to the results in section 6b. As described in section 4, surface emissivity values for the test cases are assigned according to the surface temperature conditions and are derived from the surface emissivity values given in Huang et al. (2016). The clear-sky OE retrieval statistics (Fig. 11) that use these surface emissivity values are referred to as "unperturbed emissivity" values in Fig. 12. Perturbations to these surface emissivity values in the OE retrieval tests must be representative of the expected uncertainty such that forward model error can be properly estimated.

The spectral emissivity retrieval developed by Xie et al. (2022), which uses 14 distinct TIRS channels in spectral regions where the polar atmosphere is at least partially transparent, reports the respective RMSE at each channel. Here we use this 1-sigma uncertainty to perturb the surface emissivity with correlated error and a scale length of four channels. The change in the standard deviation of the residuals for the temperature profile are essentially unchanged (not shown), whereas there is an increase in the surface temperature residual variability is approximately doubled from 0.19 to 0.40 K. There is a small increase, compared to the unperturbed values, in the standard deviation of the residuals of the log Q profiles near the surface and thus also for the CWV values (Fig. 12). The standard deviation of the CWV residuals increases from 0.33 to 0.36 cm, indicating that the uncertainty in assumed surface emissivity could increase the CWV retrieval uncertainty by 9%.

2) Exploring possible cloud induced error

Water vapor retrievals that rely on cloud masks to screen out cloudy scenes are susceptible to optically thin clouds affecting the spectra of a scene deemed to be "clear sky." Conventional satellite MIR retrievals must also account for cloud presence to retrieve atmospheric properties (Susskind et al. 2003). The Arctic Ocean region data are used to estimate the influence of optically thin ice clouds from a statistical perspective. An ice cloud at 506 hPa with a specified optical depth is modeled using PCRTM, producing a radiance spectrum that is altered from the corresponding clear-sky values, thus leading to error in the atmospheric OE retrieval. The presence of an ice cloud leads to biases in the temperature profile, both at the surface and in the lower troposphere (Fig. 13b). Figure 13a indicates that the standard deviation of the residuals for the temperature profile is mainly increased near and at the surface for larger cloud optical depths. The result being that the reported uncertainty will be greatly underestimated for the surface temperature as indicated by large standard deviation of the scaled surface temperature residuals (Fig. 13c).

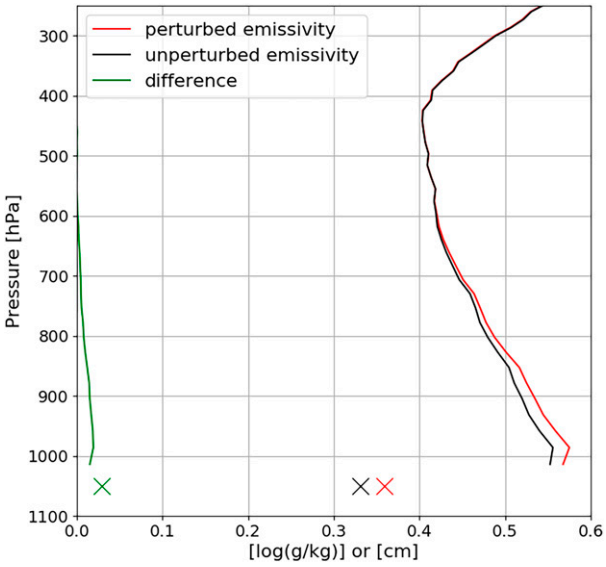

FIG. 12. The standard deviation of the log(Q) residuals [log(g kg^{-1})] and CWV residuals (cm) for the Arctic Ocean region. The unperturbed OE retrieval statistics (black line) are the baseline values in Fig. 11a, and the perturbed statistics (red line) are calculated using representative surface emissivity uncertainty. Residuals are retrieved − "truth" values. The difference (green) is the perturbed minus the unperturbed statistics.

The presence of an ice cloud leads to biases in the moisture profile, although this bias changes from positive in the midtroposphere to negative near the surface and at upper atmospheric pressures (Fig. 14b). In addition, these high level ice clouds affect the standard deviation of the Q residuals in the lower troposphere. For a cloud optical depth of 0.2 the variability of the residuals is 0.6 log(g kg^{-1}) at around 900 hPa (Fig. 14a), which is equivalent to the standard deviation of the prior. For an increase in cloud optical depth there is an increase in the standard deviation of the CWV residuals (Fig. 14a). For a cloud optical depth of 0.1, 0.2, 0.3, 0.5 the variability is enhanced nonlinearly to 0.38, 0.45, 0.55, and 0.81 cm, compared to a clear-sky value of 0.33. The variability of the residuals scaled by the reported uncertainty (Fig. 14c) indicates undetected clouds that are not flagged as cloudy scenes can introduce error such that the reported uncertainty is not equal to actual uncertainty, resulting in a ratio that is greater than unity. The impact of clouds on the 7-layer combined retrievals are similar to the full 101-level retrievals for both the temperature and Q (not shown). A PREFIRE cloud mask described by Bertossa et al. (2023) estimates that scenes with cloud optical depths greater than 0.15 will be flagged as

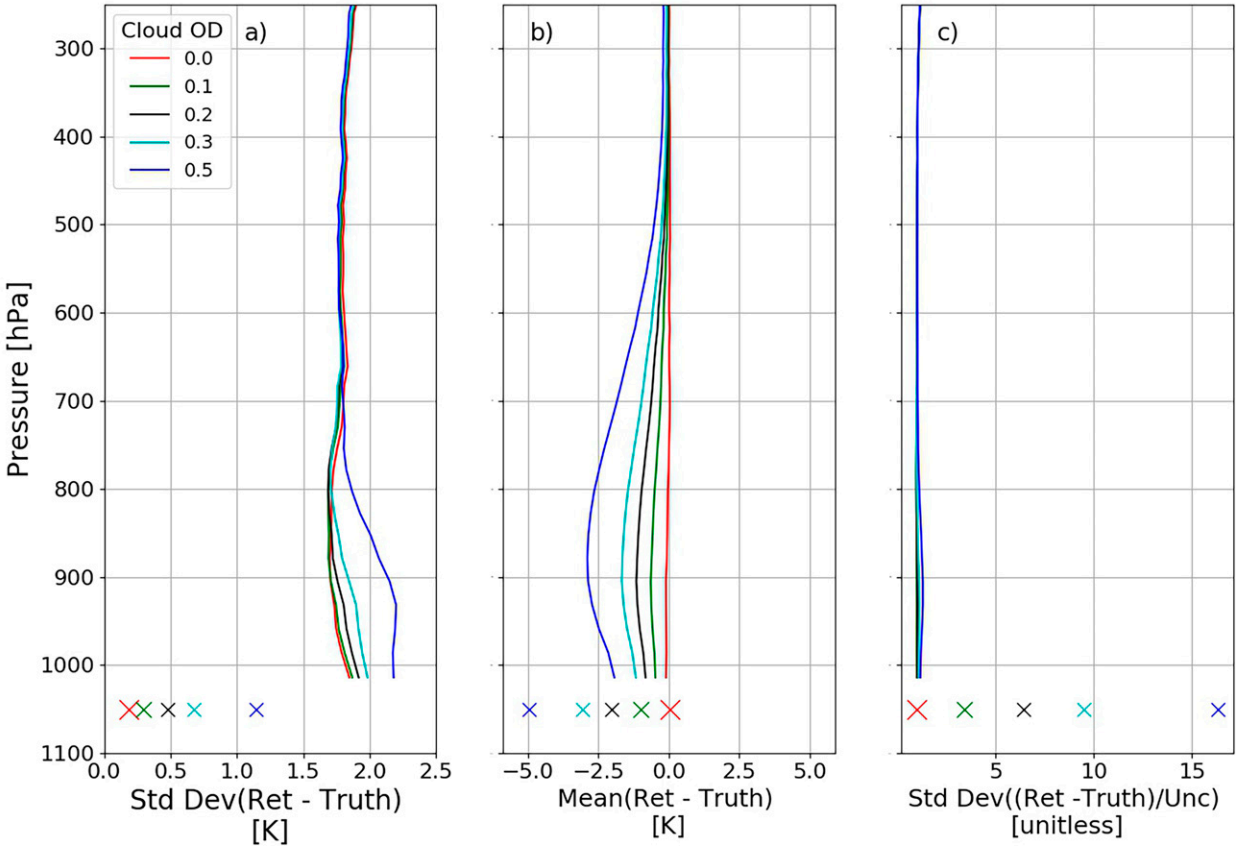

FIG. 13. Temperature retrieval statistics, in the Arctic Ocean region, for ice clouds at 506 hPa with four different cloud optical depth (cod) values, compared to the clear-sky values (red). The statistics include (a) the standard deviation of the residuals (K), (b) the mean of the residuals (K), and (c) the standard deviation of residual scaled by the reported uncertainty (unitless). Residuals are retrieved − "truth" values. The surface temperature values (K) are shown by the markers located at 1050 hPa.

cloudy with an 85% accuracy as evaluated with simulated data, limiting the error caused by cloud presence.

The OE retrieval outputs two metrics that can be used to indicate the how trustworthy the reported state variables and associated uncertainty are and may provide a means for identifying undetected cloud-affected retrievals. Reduced χ^2 is indicative of whether the retrieved state matches the measured radiance within the instrument noise level. Figure 15a shows that the clear-sky reduced χ^2 distribution is centered on approximately 1. As the ice cloud become more optically thick the distribution is shifted and skewed toward larger reduced χ^2 values. Using the reduced χ^2 metric would filter out questionable retrievals above a selected threshold (e.g., Elsaesser and Kummerow 2008), but will not guarantee that the values below this threshold are uncontaminated by cloud presence. Other metrics could be used in conjunction such as the number of iterations (Fig. 15b). The simulated data used here indicate 3 iterations may be a good threshold to flag the retrieval as questionable, yet the in-orbit retrieval may have different clear-sky convergence characteristics not captured in the simulation, so these metrics will need to be investigated postlaunch.

7. Conclusions

PREFIRE is a NASA Earth Ventures mission to measure the complete spectral range of Earth's thermal emission from polar orbit. The TIRS instruments provide moderate spectral resolution observations in a compact payload, installed on two separate CubeSat spacecraft. The PREFIRE mission will collect the first FIR spaceborne observations in over 40 years, using proven detector technology, with the goal of providing at least one complete year of global data. The results and retrieval techniques that emerge out of the PREFIRE endeavors provide a solid foundation for future missions and advance our understanding of the outgoing FIR emission, enhancing our ability to characterize the total energy balance of Earth.

The OE retrieval of temperature, humidity, CWV, and surface temperature is evaluated in four test regions which include polar regions within the Arctic Ocean, central Greenland, and Antarctica, with an additional area in the tropical Pacific Ocean. Calculating the degrees of freedom for signal (DFS), using PCRTM as the forward model, quantifies the information content, indicating that the total DFS increases with an increase in CWV. This trend is apparent in the average

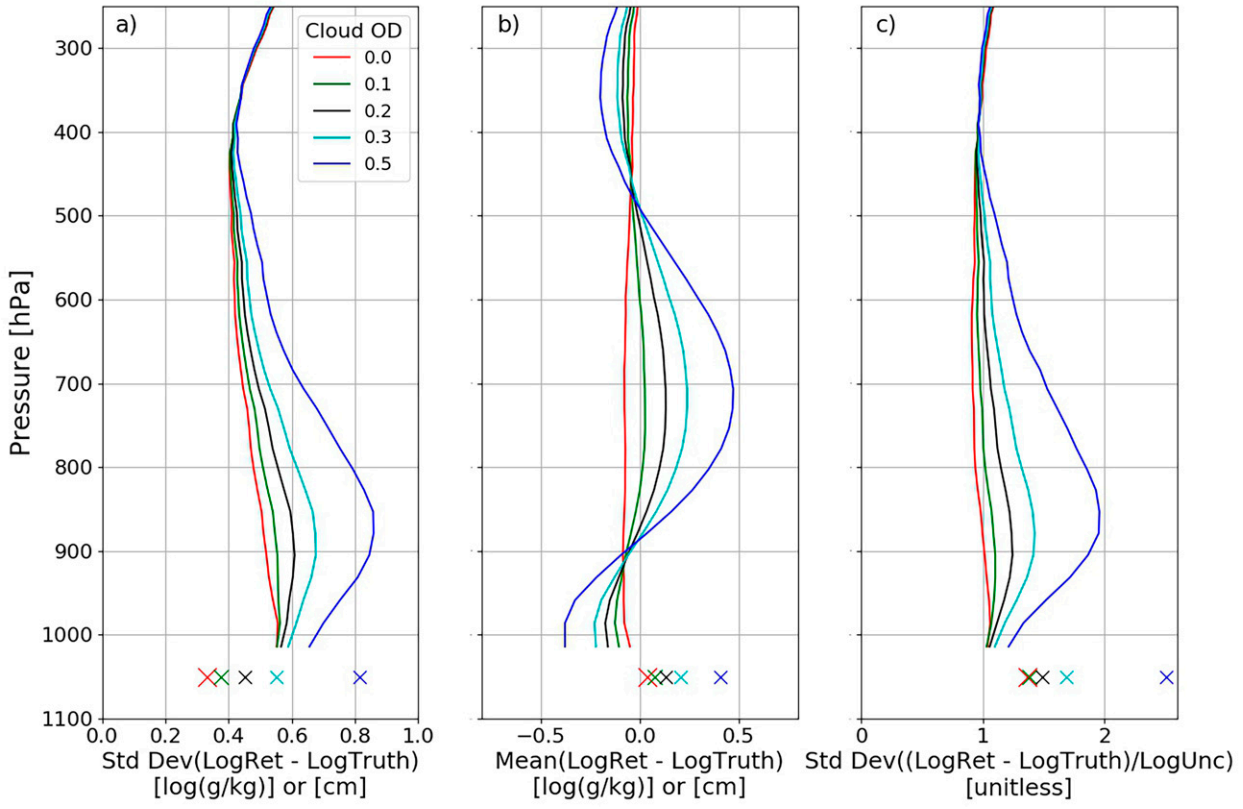

FIG. 14. Specific humidity retrieval statistics, in the Arctic Ocean region, for ice clouds at 506 hPa with four different cloud optical depth (cod) values, compared to the clear-sky values (red). The statistics include (a) the standard deviation of the residuals [log(g kg^{-1})], (b) the mean of the residuals [log(g kg^{-1})], and (c) the standard deviation of residual scaled by the reported uncertainty (unitless). Residuals are retrieved − "truth" values. The CWV values (cm) are shown by the markers located at 1050 hPa.

total DFS values for the four regions, wherein the drier and higher elevation regions have lower information content. Another factor that increases the total DFS is the presence of near-surface temperature inversions, which occur more frequently in the drier conditions.

Specific TIRS channels will have more of an impact on enhancing the total DFS than other channels. Ranking the channels according to the information content indicates that the highest ranked TIRS channels are centered at 5.9, 12.7, 18.6, and 21.1 μm. For the Arctic Ocean region the FIR channels

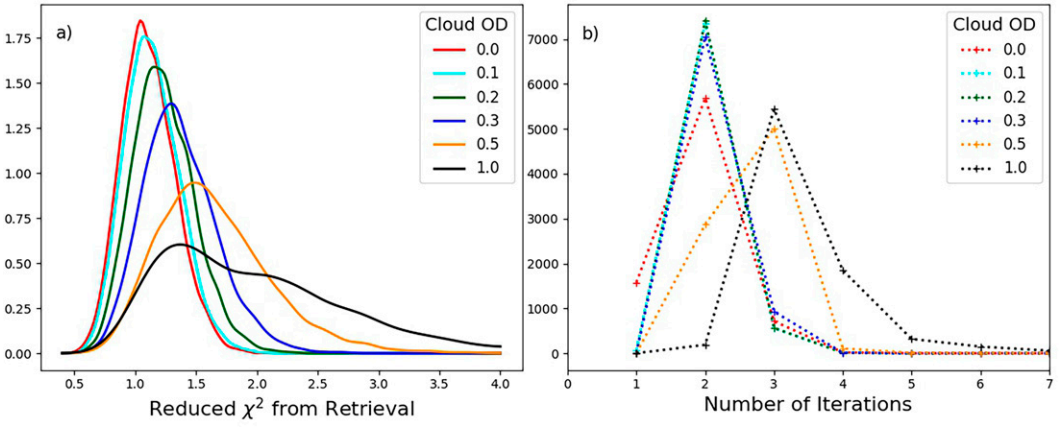

FIG. 15. Arctic Ocean region retrieval metrics for sensitivity tests of ice clouds at 506 hPa with four different cloud optical depth (OD) values, compared to the clear-sky values (red). The OE retrieval metrics include (a) reduced χ^2 and (b) the number of iterations needed to converge.

(18.6 and 21.1 μm) are ranked first more often than both the mid-IR channel (12.7 μm) and near-IR channel (5.9 μm), indicating the importance of the FIR. The FIR channels greater than 31 μm generally have a low channel rank due, in part, to the predicted low signal-to-noise ratio of the TIRS instrument at these longer wavelengths. The substantial contribution to the information content of the 16–29 μm FIR channels underlines the utility of FIR measurements in retrieving temperature and moisture profiles, in agreement with Merrelli and Turner (2012).

The total DFS is nonuniformly distributed throughout the atmospheric profile on the full resolution levels used by the PCRTM radiative transfer model. By combining the full resolution levels, a coarse 7-layer profile is produced with more equal vertical distribution of DFS. The advantage of this level combining technique is evident in looking at the statistics wherein the standard deviation of residuals are reduced for the 7-layer output. Hence, an increase in layer DFS translates to a reduction in the differences between the retrieved and actual atmospheric state at the coarser vertical resolution. The column integrated water vapor variability as a percentage of mean CWV increases for the drier regions, which corresponds to smaller total DFS in these regions.

The clear-sky atmospheric retrieval relies on a cloud mask and an estimate of the surface emissivity as input. Like all infrared sounding retrievals, undetected high-level ice clouds will increase the bias of both the temperature and humidity profile estimates. In addition, the reported uncertainty will be underestimated in the presence of thin ice clouds, especially in regard to the retrieved surface temperature. The impact of the surface emissivity retrieval uncertainty is relatively small, contributing primarily to an increase in variability of the surface temperature residuals by about a factor of 2. The effect on the column water vapor retrieval is smaller since the increase in the standard deviation of the CWV residuals amounts to about 9%.

Since the present study uses simulated observations, the quantitative assessments made here will need to be reevaluated with retrievals from real observations and comparison to independent datasets. A thorough evaluation of the performance and documentation of any operational adjustments to the retrieval algorithm will be discussed in future work.

This PREFIRE atmospheric OE retrieval will be a valuable tool for estimating water vapor profiles and CWV using far-IR measurements. The retrieved amount of water vapor in the atmospheric column feeds back into the surface emissivity retrieval, which will provide a new perspective on the spectral signatures of surface emissivity in the Arctic and Antarctica. The feasibility of utilizing the FIR is demonstrated for temperature and water vapor retrievals and the anticipated success of PREFIRE will lay the groundwork for future missions to come.

Acknowledgments. This work was supported by NASA under the Earth Ventures-Instrument (EV-I) program's Polar Radiant Energy in the Far Infrared Experiment (PREFIRE) mission. Components of the work performed at the University of Wisconsin–Madison and University of Michigan were supported under the associated NASA PREFIRE Grant 80NSSC18K1485. Portions of this research were carried out at the Jet Propulsion Laboratory, California Institute of Technology, under contract with the National Aeronautics and Space Administration.

Data availability statement. The ERA5 data were obtained online (https://apps.ecmwf.int/data-catalogues/era5).

REFERENCES

Bertossa, C., T. L'Ecuyer, A. Merrelli, X. Huang, and X. Chen, 2023: A neural network–based cloud mask for PREFIRE and evaluation with simulated observations. *J. Atmos. Oceanic Technol.*, **40**, 377–396, https://doi.org/10.1175/JTECH-D-22-0023.1.

Chang, K.-W., T. S. L'Ecuyer, B. H. Kahn, and V. Natraj, 2017: Information content of visible and midinfrared radiances for retrieving tropical ice cloud properties. *J. Geophys. Res. Atmos.*, **122**, 4944–4966, https://doi.org/10.1002/2016JD026357.

Chen, B., and Z. Liu, 2016: Global water vapor variability and trend from the latest 36 year (1979 to 2014) data of ECMWF and NCEP reanalyses, radiosonde, GPS, and microwave satellite. *J. Geophys. Res. Atmos.*, **121**, 11 442–11 462, https://doi.org/10.1002/2016JD024917.

Di, D., Y. Ai, J. Li, W. Shi, and N. Lu, 2016: Geostationary satellite-based 6.7 μm band best water vapor information layer analysis over the Tibetan Plateau. *J. Geophys. Res. Atmos.*, **121**, 4600–4613, https://doi.org/10.1002/2016JD024867.

Durre, I., R. S. Vose, and D. B. Wuertz, 2006: Overview of the Integrated Global Radiosonde Archive. *J. Climate*, **19**, 53–68, https://doi.org/10.1175/JCLI3594.1.

Elsaesser, G. S., and C. D. Kummerow, 2008: Toward a fully parametric retrieval of the nonraining parameters over the global oceans. *J. Appl. Meteor. Climatol.*, **47**, 1599–1618, https://doi.org/10.1175/2007JAMC1712.1.

Errico, R. M., and N. C. Privé, 2014: An estimate of some analysis-error statistics using the Global Modeling And Assimilation Office observing-system simulation framework. *Quart. J. Roy. Meteor. Soc.*, **140**, 1005–1012, https://doi.org/10.1002/qj.2180.

Feldman, D. R., W. D. Collins, R. Pincus, X. Huang, and X. Chen, 2014: Far-infrared surface emissivity and climate. *Proc. Natl. Acad. Sci. USA*, **111**, 16 297–16 302, https://doi.org/10.1073/pnas.1413640111.

Hanel, R. A., B. Schlachman, F. D. Clark, C. H. Prokesh, J. B. Taylor, W. M. Wilson, and L. Chaney, 1970: The Nimbus III Michelson interferometer. *Appl. Opt.*, **9**, 1767–1774, https://doi.org/10.1364/AO.9.001767.

——, ——, D. Rogers, and D. Vanous, 1971: Nimbus 4 Michelson interferometer. *Appl. Opt.*, **10**, 1376–1382, https://doi.org/10.1364/AO.10.001376.

Hersbach, H., and Coauthors, 2020: The ERA5 global reanalysis. *Quart. J. Roy. Meteor. Soc.*, **146**, 1999–2049, https://doi.org/10.1002/qj.3803.

Hilton, F., and Coauthors, 2012: Hyperspectral Earth observation from IASI: Five years of accomplishments. *Bull. Amer. Meteor. Soc.*, **93**, 347–370, https://doi.org/10.1175/BAMS-D-11-00027.1.

Huang, X., X. Chen, D. K. Zhou, and X. Liu, 2016: An observationally based global band-by-band surface emissivity dataset

for climate and weather simulations. *J. Atmos. Sci.*, **73**, 3541–3555, https://doi.org/10.1175/JAS-D-15-0355.1.

Kempe, V., D. Oertel, R. Schuster, H. Becker-Ross, and H. Jahn, 1980: Absolute IR-spectra from the measurement of Fourier-spectrometers aboard *Meteor 25* and *28*. *Acta Astronaut.*, **7**, 1403–1416, https://doi.org/10.1016/0094-5765(80)90015-6.

L'Ecuyer, T. S., P. Gabriel, K. Leesman, S. J. Cooper, and G. L. Stephens, 2006: Objective assessment of the information content of visible and infrared radiance measurements for cloud microphysical property retrievals over the global oceans. Part I: Liquid clouds. *J. Appl. Meteor. Climatol.*, **45**, 20–41, https://doi.org/10.1175/JAM2326.1.

——, and Coauthors, 2021: The Polar Radiant Energy in the Far Infrared Experiment: A new perspective on polar longwave energy exchanges. *Bull. Amer. Meteor. Soc.*, **102**, E1431–E1449, https://doi.org/10.1175/BAMS-D-20-0155.1.

Lerner, J. A., E. Weisz, and G. Kirchengast, 2002: Temperature and humidity retrieval from simulated Infrared Atmospheric Sounding Interferometer (IASI) measurements. *J. Geophys. Res.*, **107**, 4189, https://doi.org/10.1029/2001JD900254.

Liu, X., W. L. Smith, D. K. Zhou, and A. Larar, 2006: Principal component-based radiative transfer model for hyperspectral sensors: Theoretical concept. *Appl. Opt.*, **45**, 201–209, https://doi.org/ 10.1364/AO.45.000201.

Lucchesi, R., 2015: File specification for GEOS-5 FP-IT. GMAO Office Note 2, version 1.4, 64 pp., https://gmao.gsfc.nasa.gov/pubs/docs/Lucchesi865.pdf.

Maahn, M., D. D. Turner, U. Löhnert, D. J. Posselt, K. Ebell, G. G. Mace, and J. M. Comstock, 2020: Optimal estimation retrievals and their uncertainties: What every atmospheric scientist should know. *Bull. Amer. Meteor. Soc.*, **101**, E1512–E1523, https://doi.org/10.1175/BAMS-D-19-0027.1.

Maddy, E. S., and C. D. Barnet, 2008: Vertical resolution estimates in version 5 of AIRS operational retrievals. *IEEE Trans. Geosci. Remote Sens.*, **46**, 2375–2384, https://doi.org/10.1109/TGRS.2008.917498.

McClatchey, R. A., R. W. Fenn, J. E. A. Selby, F. E. Volz, and J. S. Garing, 1972: Optical properties of the atmosphere. Air Force Cambridge Research Laboratories Tech. Rep. AFCRL-72-0497, 113 pp., https://apps.dtic.mil/sti/citations/AD0753075.

Menzel, W. P., T. J. Schmit, P. Zhang, and J. Li, 2018: Satellite-based Atmospheric Infrared Sounder development and applications. *Bull. Amer. Meteor. Soc.*, **99**, 583–603, https://doi.org/10.1175/BAMS-D-16-0293.1.

Merrelli, A., and D. D. Turner, 2012: Comparing information content of upwelling far-infrared and midinfrared radiance spectra for clear atmosphere profiling. *J. Atmos. Oceanic Technol.*, **29**, 510–526, https://doi.org/10.1175/JTECH-D-11-00113.1.

Nalli, N. R., and Coauthors, 2013: Validation of satellite sounder environmental data records: Application to the Cross-Track Infrared Microwave Sounder Suite. *J. Geophys. Res. Atmos.*, **118**, 13 628–13 643, https://doi.org/10.1002/2013JD020436.

Palchetti, L., G. Bianchini, G. Di Natale, and M. Del Guasta, 2015: Far-infrared radiative properties of water vapor and clouds in Antarctica. *Bull. Amer. Meteor. Soc.*, **96**, 1505–1518, https://doi.org/10.1175/BAMS-D-13-00286.1.

——, and Coauthors, 2020: FORUM: Unique far-infrared satellite observations to better understand how Earth radiates energy to space. *Bull. Amer. Meteor. Soc.*, **101**, E2030–E2046, https://doi.org/10.1175/BAMS-D-19-0322.1.

Rathke, C., J. Fischer, S. Neshyba, and M. Shupe, 2002: Improving IR cloud phase determination with 20 microns spectral observations. *Geophys. Res. Lett.*, **29**, 1209, https://doi.org/10.1029/2001GL014594.

Rodgers, C. D., 1976: Retrieval of atmospheric temperature and composition from remote measurements of thermal radiation. *Rev. Geophys.*, **14**, 609–624, https://doi.org/10.1029/RG014i004p00609.

——, 2000: *Inverse Methods for Atmospheric Sounding: Theory and Practice*. World Scientific, 240 pp.

Schmit, T. J., S. S. Lindstrom, J. J. Gerth, and M. M. Gunshor, 2018: Applications of the 16 spectral bands on the Advanced Baseline Imager (ABI). *J. Oper. Meteor.*, **6**, 33–46, https://doi.org/10.15191/nwajom.2018.0604.

Serreze, M. C., A. P. Barrett, A. G. Slater, M. Steele, J. Zhang, and K. E. Trenberth, 2007: The large-scale energy budget of the Arctic. *J. Geophys. Res.*, **112**, D11122, https://doi.org/10.1029/2006JD008230.

Shahabadi, M. B., and Y. Huang, 2014: Measuring stratospheric H_2O with an airborne spectrometer. *J. Atmos. Oceanic Technol.*, **31**, 1502–1515, https://doi.org/10.1175/JTECH-D-13-00191.1.

Susskind, J., C. D. Barnet, and J. M. Blaisdell, 2003: Retrieval of atmospheric and surface parameters from AIRS/AMSU/HSB data in the presence of clouds. *IEEE Trans. Geosci. Remote Sens.*, **41**, 390–409, https://doi.org/10.1109/TGRS.2002.808236.

Turner, D. D., and E. J. Mlawer, 2010: The Radiative Heating in Underexplored Bands Campaigns. *Bull. Amer. Meteor. Soc.*, **91**, 911–924, https://doi.org/10.1175/2010BAMS2904.1.

——, and U. Löhnert, 2014: Information content and uncertainties in thermodynamic profiles and liquid cloud properties retrieved from the ground-based Atmospheric Emitted Radiance Interferometer (AERI). *J. Appl. Meteor. Climatol.*, **53**, 752–771, https://doi.org/10.1175/JAMC-D-13-0126.1.

——, S. A. Clough, J. C. Liljegren, E. E. Clothiaux, K. E. Cady-Pereira, and K. L. Gaustad, 2007: Retrieving liquid water path and precipitable water vapor from the Atmospheric Radiation Measurement (ARM) microwave radiometers. *IEEE Trans. Geosci. Remote Sens.*, **45**, 3680–3690, https://doi.org/10.1109/TGRS.2007.903703.

Warwick, L., and Coauthors, 2022: Retrieval of tropospheric water vapor from airborne far-infrared measurements: A case study. *J. Geophys. Res. Atmos.*, **127**, e2020JD034229, https://doi.org/10.1029/2020JD034229.

Xie, Y., X. Huang, X. Chen, T. S. L'Ecuyer, B. J. Drouin, and J. Wang, 2022: Retrieval of surface spectral emissivity in polar regions based on the optimal estimation method. *J. Geophys. Res. Atmos.*, **127**, e2021JD035 677, https://doi.org/10.1029/2021JD035677.

Zhang, Y., D. J. Seidel, J.-C. Golaz, C. Deser, and R. A. Tomas, 2011: Climatological characteristics of Arctic and Antarctic surface-based inversions. *J. Climate*, **24**, 5167–5186, https://doi.org/10.1175/2011JCLI4004.1.